Reviews in Mineralogy & Geochemistry
Vol. 86 pp. 197–216, 2021

Mass-Independent Fractionation of Oxygen Isotopes in the Atmosphere

Marah Brinjikji and James R. Lyons

School of Earth & Space Exploration
Arizona State University
550 East Tyler Mall, PSF 686
Tempe, AZ 85287
USA

mbrinjik@asu.edu

jimlyons@asu.edu

INTRODUCTION

We review the O isotope modeling in the atmosphere below 100 km, which is a large and active area of research. Our review will not be exhaustive but instead will highlight some of the key papers on the topic over the past nearly 30 years. We focus our review on modeling the mass-independent fractionation signatures associated with O_3 formation and other species that photochemically interact with O_3. After a brief discussion of isotopic O_3 formation, we present results from models of $\Delta^{17}O$ in CO_2, OH and H_2O, nitrates, sulfates, and in pollution in urban environments.

We then present new O isotope results for the atmosphere above 100 km. There are presently no oxygen isotope measurements for Earth's atmosphere above about 60 km (Thiemens 1995). Here, we present model results for the oxygen isotope composition of Earth's thermosphere and ionosphere using a 1-D photochemical model. This work was motivated by the NASA MAVEN mission, which is studying ion and neutral composition, and escape fluxes from, the thermosphere of Mars, and includes isotopic species (Jakosky 1994; Jakosky et al. 2017, 2018). The realization that comparable isotopic measurements for Earth's thermosphere are lacking prompted our study.

PREVIOUS WORK IN THE LOWER ATMOSPHERE

Early measurements

Because our main interest here is in mass-independent fractionation (MIF) of O isotopes, or, as will be seen for the upper atmosphere, *apparent* MIF, we will not review the large literature on O and H isotopes of atmospheric water vapor, and the influence of exchange with soils, which has been a topic of ongoing research for many decades. We begin with the stratospheric work of Konrad Mauersberger. Using a balloon platform, Mauersberger (1981) performed *in situ* mass spectrometry of O_3 in the stratosphere, discovering an enormous enrichment of ~ 400‰ in $^{16}O^{16}O^{18}O$ (mass 50). We now know that this value is too high, but, qualitatively, the discovery was made. In the laboratory the key discovery of mass-independent fractionation was made by Thiemens and Heidenreich (1983) by passing an electric discharge through O_2 in a flask, and measuring the O isotope composition of the O_3 produced and the residual O_2. Instead of the usual mass-dependent isotope behavior (adhering to the slope of ~0.5 in $^{17}O/^{16}O$ vs. $^{18}O/^{16}O$ coordinates), they found that the O_2 and O_3 defined a line of nearly slope 1 on 3-isotope space, leading to the term 'mass-independent' fractionation. It is difficult to overstate the significance

1529-6466/21/0086-0006$05.00 (print)
1943-2666/21/0086-0006$05.00 (online)
http://dx.doi.org/10.2138/rmg.2021.86.06

of this experiment on our understanding of atmospheric O isotopes. Ozone participates in a wide variety of oxygen chemical reactions, either directly as O_3 or as a source of $O(^1D)$, which forms OH upon reaction with water vapor. In this manner, MIF inherited from O_3 manifests itself in nearly all O-containing compounds in the atmosphere (Lyons 2001).

Continued isotopic measurements in the laboratory and in the atmosphere confirmed the original discovery (Thiemens and Heidenreich 1983), and sought to clarify the mechanism responsible for the unusual isotopic behavior of O_3. Analyses of O_3 were made in both the troposphere and stratosphere (e.g., Krankowsky et al. 1995, 2000; Johnston et al. 1997). Laboratory studies focused on O_3 formation reactions under a variety of conditions (e.g., Morton et al. 1990, Janssen et al. 1999), culminating in measured rate coefficients for formation of isotopic O_3 (Mauersberger et al. 1999). Other studies discovered oxygen MIF effects in other relevant atmospheric reactions (Röckmann et al. 1998; Savarino and Thiemens 1999). Although much smaller in magnitude than the O_3 MIF signature, these latter reactions are still informative from a chemical physics perspective.

Theory and photochemical modeling of O_3 MIF signatures

Photochemical models began exploring the implications of heavy ozone in the atmosphere, even though there was essentially no isotopic rate coefficient data available, and even the reaction responsible for O_3 was debated. An early successful model looked at stratospheric CO_2, and recognized that $O(^1D)$, produced from O_3 photolysis, will form the metastable CO_3 (Yung et al. 1991). Breakup of the CO_3 imparts an O_3-derived MIF signature to the CO_2, diminished by the probability of ^{17}O or ^{18}O remaining in the CO_2. This mechanism-based analysis of the transfer of O_3 MIF to another molecule, namely stratospheric CO_2, demonstrated both the significance and subtlety with which O_3 can impart isotopic signatures to other molecules. With the measurement of isotopic rate coefficients by Mauersberger et al. (1999), it became possible to more quantitatively model O isotope exchange processes in the atmosphere. Lyons (2001) investigated transfer of O_3 MIF signatures to about 10 other molecules, and provided some unification for the expected oxygen isotope composition of the troposphere and stratosphere.

The measurement of the isotopic rate coefficients by Mauersberger et al. (1999) also made it possible for the physical chemists to quantitatively investigate the mechanism responsible for O_3 MIF. A series of papers from Rudy Marcus's group (Hathorn and Marcus 2000; Gao and Marcus 2002) provided a semi-empirical, and extremely useful, theory for understanding the role of zero-point energy and symmetry in the wide range of isotopic rate coefficient values for O_3 formation. The MIF signature derived from non-statistical behavior in the asymmetric O_3 isotopomers, the exact physical origin of which is still being explored. Importantly for the photochemical modelers, the Marcus formulation allowed prediction of unmeasured rate coefficients. This is particularly important for the mixed-isotope O_2 species, e.g., $^{16}O^{17}O$ and $^{16}O^{18}O$, whose reactions with ^{16}O are essential in the atmosphere but difficult to measure in the laboratory.

Applications of oxygen MIF

Ozone MIF signatures (i.e., enhancements or depletions in ^{17}O) have had a tremendous range of application in geochemistry, both for the modern and ancient Earth. We will not attempt to review all of these applications, but will mention a few that we think are especially notable, with the recognition that we are not without bias. Many of the most significant applications of oxygen MIF have been to measures of global primary productivity (GPP), as first pointed out by Bender et al. (1994). Accurate measurements of the MIF signature of O_2 allowed Luz et al. (1999) to relate modern primary productivity to the cross-tropopause transport timescales for air. The small negative MIF signature in bulk tropospheric O_2 with $\Delta^{17}O \sim -0.2‰$, results from the storage of a positive MIF signature in stratospheric CO_2 via transfer from O_3 by the excited state atom $O(^1D)$ (Yung et al. 1991). This powerful technique has also been applied to O_2 collected from Antarctic ice and snow, extending productivity estimates back to the middle ages (Savarino et al. 2003).

One of the most remarkable MIF-related discoveries is that of negative MIF signatures, $\Delta^{17}O \sim -0.8$ to $-1.6‰$ in sulfates from the Cryogenian period (Bao et al. 2008). Reconstructing the implied isotopic composition for O_2 yields $\Delta^{17}O \sim -2$ to $-6‰$. By accounting for the efficiency of subaerial pyrite oxidation, the exact same mechanism invoked by Luz et al. (1999) may be applied to this much earlier geological period to place a constraint on atmospheric CO_2. Given plausible assumptions about productivity at that time, greatly elevated levels of CO_2 may be inferred (up to 30 times the modern value), just as predicted for the aftermath 'hothouse' following the end of a Snowball Earth glaciation (Bao et al. 2008). Most recently, Hodgkiss et al. (2019) used $\Delta^{17}O$ values of sulfate (also $\sim -0.8‰$) to argue for the collapse of productivity at the end of the great oxidation event (GOE). Because the sulfate $\Delta^{17}O$ values depend on pO_2, pCO_2, and GPP, different interpretations are possible for the Snowball Earth and the GOE.

There are numerous other applications of O isotope MIF signatures, some of which are discussed in more detail below. These include atmospherically-derived nitrates such as those in the Atacama desert in Chile (Michalski et al. 2004), the origin of desert varnish on rocks (Bao et al. 2001), and an improved quantification of stratospheric volcanism (Gautier et al. 2019). Additionally, oxygen MIF signatures have been investigated for polar water vapor (Lin et al. 2013), stratospheric CO_2 (Liang et al. 2007), and the sulfate formation mechanism in marine sea-salt aerosols (Alexander et al. 2005). The breadth of applications of O_3 MIF signatures are a testament to the importance of the phenomenon.

MATERIALS AND METHODS

VULCAN photochemical model

VULCAN is a 1-D chemical kinetics model developed for high-temperature exoplanet atmospheres (Tsai et al. 2017). The original version of VULCAN utilized a reduced C–H–O chemical network consisting of about 300 gas-phase reactions valid in a 500–2500 K temperature range. However, the code is highly general, and is readily adapted to low-temperature atmospheres, as well as atmospheres with N and S-containing molecular species. We have adapted VULCAN to the Earth thermosphere and ionosphere, and with the inclusion of O isotopes. VULCAN solves a system of vertical 1-D continuity equations (Eqn. 1) using a Rosenbrock solver (Tsai et al. 2017). The Rosenbrock solver has been shown to be highly effective for systems of 'stiff' ordinary differential equations, such as occur in atmospheric chemical kinetics. Vertical transport due to both eddy and molecular diffusion is represented by a vertical diffusion equation. For high-temperature atmospheres, reverse reaction rate coefficients are computed from a measured forward rate, combined with the equilibrium constant for the reaction. The equilibrium constant is computed from the Gibbs free energy of the reaction, adjusted for pressures (Tsai et al. 2017). To model Earth's atmosphere, we have turned off the reverse reactions. We have done this even for the thermosphere because the kinetics of the relevant neutral–neutral and ion–molecule reactions are well known from decades of laboratory work (e.g., Brasseur and Solomon 1984). The isotopic reactions are less well studied, but we assume that they do not differ greatly from the reactions of the dominant ^{16}O isotope. For reactions involving O_3 in the lower atmosphere, such an assumption is incorrect due to the non-statistical nature of O_3 recombination reactions (Gao and Marcus 2002). In the thermosphere, O_3 formation is unimportant, and we assume that the isotopic reaction rate coefficients are independent of isotope, apart from a mass-dependent reduced-mass factor discussed further below.

The continuity equations solved in VULCAN are given by

$$\frac{dn_i}{dt} + \frac{d\phi_i}{dt} = P_i - L_i \tag{1}$$

where n_i and f_i are the number density (cm^{-3}) and vertical flux ($cm^{-2}\ s^{-1}$) for species i in the model. P_i and L_i are the production and loss rates ($cm^{-3}\ s^{-1}$) for species i due to chemical and photodissociation reactions. The vertical flux satisfies a 1st-order diffusion equation,

$$\phi_i = -D_i\left(\frac{dn_i}{dz} + \frac{n_i}{H_i}\right) - K\left(\frac{dn_i}{dz} + \frac{n_i}{H_a}\right) \tag{2}$$

where D_i is the molecular diffusion coefficient for species i diffusing through the background atmosphere, and K is the vertical eddy diffusion coefficient applicable to all species. The scale height of species i is

$$H_i = \frac{kT}{m_i g} \tag{3}$$

and for the well-mixed atmosphere is

$$H_a = \frac{kT}{m_a g} \tag{3b}$$

for mean molecular mass, m_a. The homopause is defined as the height at which $D_i \sim K$ for most species. Above this height, which is about 100 km for Earth, molecular diffusion dominates over eddy diffusion. Here, eddy diffusion means mixing by eddies on the full range of size scales from the Kolmogorov microscale to the scale height of the bulk atmosphere, H_a. The occurrence of m_i in Equation (3a), and not in Equation (3b), is the basis of diffusive separation in the thermosphere.

RESULTS FOR THE LOWER ATMOSPHERE

We present a short synopsis of O isotopes in the lower atmosphere based on the photochemical equilibrium calculations in Lyons (2001), and then discuss more recent work on modeling MIF signatures in O_3, CO_2, H_2O, nitrates, sulfates, and O-containing components of air pollution. The focus of Lyons (2001) was the transfer of O_3 MIF signatures to other oxygen-containing molecules in the atmosphere. We summarize this work below, and present updated results for $\Delta^{17}O$ of several lower atmosphere species.

The relevant isotopic O_3 formation reactions are the following:

$$O + O_2 \xrightarrow{M} O_3 \qquad k_1 \tag{R1}$$

$$Q + O_2 \xrightarrow{M} QOO \qquad k_2 \tag{R2}$$

$$O + QO \xrightarrow{M} QOO \qquad k_3\gamma_Q \tag{R3a}$$

$$O + QO \xrightarrow{M} OQO \qquad k_3(1-\gamma_Q) \tag{R3b}$$

$$P + O_2 \xrightarrow{M} POO \qquad k_4 \tag{R4}$$

$$O + PO \xrightarrow{M} POO \qquad k_5\gamma_P \tag{R5a}$$

$$O + PO \xrightarrow{M} OPO \qquad k_5(1-\gamma_P) \tag{R5b}$$

In these reactions k is the 3-body rate coefficient, γ is the branching ratio, Q = ^{18}O and P = ^{17}O, and M is a 3rd-body collision partner, usually O_2 or N_2. The primary loss for ozone is photodissociation. There are multiple photodissociation channels, but, for the purpose of illustration, we only consider the channel forming $O(^1D)$. We also assume the photodissocation rate constants are

identical for all isotopomers of O_3. This is not exactly correct, but it simplifies the resulting equations. The resulting photodissociation reactions are shown in reactions (R6–R10).

$$O_3 + h\nu \rightarrow O(^1D) + O_2 \qquad J_1 \tag{R6}$$

$$QOO + h\nu \rightarrow O(^1D) + QO \qquad \tfrac{1}{2}J_1 \tag{R7a}$$

$$QOO + h\nu \rightarrow Q(^1D) + O_2 \qquad \tfrac{1}{2}J_1 \tag{R7b}$$

$$OPO + h\nu \rightarrow O(^1D) + PO \qquad J_1 \tag{R8}$$

$$POO + h\nu \rightarrow O(^1D) + PO \qquad \tfrac{1}{2}J_1 \tag{R9a}$$

$$POO + h\nu \rightarrow P(^1D) + O_2 \qquad \tfrac{1}{2}J_1 \tag{R9b}$$

$$OPO + h\nu \rightarrow O(^1D) + PO \qquad J_1 \tag{R10}$$

We must also include O exchange with O_2:

$$Q + O_2 \rightarrow QO + O \qquad k_{6f} \tag{R11a}$$

$$O + QO \rightarrow Q + O_2 \qquad k_{6r} \tag{R11b}$$

$$P + O_2 \rightarrow PO + O \qquad k_{7f} \tag{R12a}$$

$$O + PO \rightarrow P + O_2 \qquad k_{7r} \tag{R12b}$$

Finally, we include quenching of the electronically excited $O(^1D)$ by collision with O_2 and N_2 to produce a ground state O atom. For the presentation here we will not include this reaction, but will simply assume that all $O(^1D)$ is rapidly quenched to O. This is, of course, not actually the case in the atmosphere, as $O(^1D)$ is involved in essential reactions with H_2O (to form OH), CO_2 (isotope exchange), and many other molecules. However, this assumption does not significantly affect the isotopic composition of O_3.

From the above set of reactions, and assuming $O(^1D) \rightarrow O$ proceeds rapidly, we may derive expressions for the O_3 isotopomer number densities and delta-values. We do this by setting production and loss rates equal to each other for a given species, and then solving for the species number densities. This will only be valid for short-lived species that are essentially not affected by transport, i.e., species in photochemical steady state. From reaction (R11) and (R12), we find

$$\frac{[Q]}{[O]} = \frac{1}{K_{eq}^{Q}} \frac{[QO]}{[O_2]} \tag{4}$$

$$\frac{[P]}{[O]} = \frac{1}{K_{eq}^{P}} \frac{[PO]}{[O_2]} \tag{5}$$

In Equations (4) and (5) $K_{eq}^{Q} = k_{6f}/k_{6r} = 1.9463e^{31.6/T}$ and $K_{eq}^{P} = k_{7f}/k_{7r} = 1.9728e^{15.8/T}$, where T is atmospheric temperature. The equilibrium constants have been evaluated from statistical mechanics and are given in Yung et al. (1997). The forward rate constants are $k_{6f} = k_{7f} = 3.4 \times 10^{-12}(300/T)^{1.1}$, neglecting reduced factors in the rate of reaction.

Again, assuming photochemical equilibrium, we derive approximate expressions for the O_3 isotopomer number densities:

$$\frac{[\mathrm{OQO}]}{[\mathrm{O_3}]} = \frac{k_3}{k_1}(1-\gamma_\mathrm{Q})\frac{[\mathrm{QO}]}{[\mathrm{O_2}]} \tag{6}$$

$$\frac{[\mathrm{QOO}]}{[\mathrm{O_3}]} = \left(\frac{k_2}{k_1}\frac{1}{K_\mathrm{eq}^\mathrm{Q}} + \frac{k_3}{k_1}\gamma_\mathrm{Q}\right)\frac{[\mathrm{QO}]}{[\mathrm{O_2}]} \tag{7}$$

$$\frac{[\mathrm{OPO}]}{[\mathrm{O_3}]} = \frac{k_5}{k_1}(1-\gamma_\mathrm{P})\frac{[\mathrm{PO}]}{[\mathrm{O_2}]} \tag{8}$$

$$\frac{[\mathrm{POO}]}{[\mathrm{O_3}]} = \left(\frac{k_4}{k_1}\frac{1}{K_\mathrm{eq}^\mathrm{P}} + \frac{k_5}{k_1}\gamma_\mathrm{P}\right)\frac{[\mathrm{PO}]}{[\mathrm{O_2}]} \tag{9}$$

The total isotopomer number densities are independent of branching ratio,

$$\frac{[\mathrm{QOO}]+[\mathrm{OQO}]}{[\mathrm{O_3}]} = \left(\frac{k_2}{k_1}\frac{1}{K_\mathrm{eq}^\mathrm{Q}} + \frac{k_3}{k_1}\right)\frac{[\mathrm{QO}]}{[\mathrm{O_2}]} \tag{10}$$

$$\frac{[\mathrm{POO}]+[\mathrm{OPO}]}{[\mathrm{O_3}]} = \left(\frac{k_4}{k_1}\frac{1}{K_\mathrm{eq}^P} + \frac{k_5}{k_1}\right)\frac{[\mathrm{PO}]}{[\mathrm{O_2}]} \tag{11}$$

Using the experimental results of Mauersberger et al. (1999) and Janssen et al. (1999), together with the semi-empirical model results of Hathorn and Marcus (2000) and Gao and Marcus (2002), we compile a table of relative rate coefficients is compiled for O_3 isotopomer formation (Table 1). The values in the 'theory' column for $\eta = 1.15$ imply $\gamma_Q = 0.594$ and $\gamma_P = 0.575$. Lyons (2001) used $\gamma_Q = \gamma_P = 0.57$ based on the incomplete experimental values. These small differences in branching ratios produce dramatically different $\Delta^{17}O$ values for the symmetric and asymmetric O_3 isotopomers, i.e., OQO and QOO, respectively. We compute delta-values as

$$\delta^x\mathrm{O}(\mathrm{O_3^s}) = \frac{[\mathrm{O}^x\mathrm{OO}]}{[\mathrm{O_3}]}\left(\frac{\mathrm{O}}{^x\mathrm{O}}\right)_\mathrm{SMOW} - 1 \tag{12}$$

$$\delta^x\mathrm{O}(\mathrm{O_3^a}) = \frac{[^x\mathrm{OOO}]}{2[\mathrm{O_3}]}\left(\frac{\mathrm{O}}{^x\mathrm{O}}\right)_\mathrm{SMOW} - 1 \tag{13}$$

$$\delta^x\mathrm{O}(\mathrm{O_3}) = \frac{[^x\mathrm{OOO}]+[\mathrm{O}^x\mathrm{OO}]}{3[\mathrm{O_3}]}\left(\frac{\mathrm{O}}{^x\mathrm{O}}\right)_\mathrm{SMOW} - 1 \tag{14}$$

Lyons (2001) assumed photochemical steady state for a system of reactions in the mid-latitude atmosphere from 0 to 60 km, analogous to Equations (6–11), but yielding a coupled non-linear system. As noted by Zahn et al. (2006), Lyons assumed $\gamma_Q = \gamma_P = 0.57$ based on the experimental data available at the time, which resulted in $\Delta^{17}O \sim -40$ to $-50‰$ for symmetric O_3 and too high a $\Delta^{17}O$ value for asymmetric O_3. Here, and below we define $\Delta^{17}O$ as

$$\Delta^{17}\mathrm{O} = (\delta^{17}\mathrm{O}+1) - (\delta^{18}\mathrm{O}+1)^\lambda \tag{15}$$

where $\lambda = 0.50–0.53$, and where the reference is VSMOW. Updated results from Lyons (2001) are shown in Figure 1. The branching ratios used in Figure 1 are $\gamma_Q = 0.594$ and $\gamma_P = 0.564$, which yields a vertically-averaged symmetric $O_3 \sim 0‰$. Temperature and pressure affect the formation rate of isotopic O_3, and although these effects were included in Lyons (2001), they have not been updated here. A more precise treatment was given in Liang et al. (2006), which we discuss further below. The key point of Figure 1 is the illustration of how O_3-derived MIF signatures are transferred to other photochemically active species.

Table 1. Relative rate coefficients for O_3 isotopomer formation.

Rate coefficient	Experiments[1]	Theory[2] (η = 1.15)	Theory[2] (η = 1.00)	Theory[3] (η = 1.18)
k_2/k_1	0.93	0.95	0.83	0.93
k_3/k_1	1.27	1.28	1.18	1.25
$k_3\gamma_Q/k_1$	0.73	0.76	0.66	0.74
$k_3(1-\gamma_Q)/k_1$	0.54	0.52	0.52	0.52
k_4/k_1	1.03	1.02	0.89	1.03
k_5/k_1	1.17	1.20	1.11	1.19
$k_5\gamma_P/k_1$	not measured	0.69	0.60	0.68
$k_5(1-\gamma_P)/k_1$	not measured	0.51	0.51	0.51

Notes:
[1] Mauersberger et al. (1999); Janssen et al. (1999).
[2] Hathorn and Marcus (2000). The parameter η characterizes the magnitude of non-statistical behavior in the asymmetric ozone isotopomers. Non-statistical behavior in a chemical reaction means a deviation from the usual Boltzmann distribution of energy levels in a microcanonical statistical mechanics description of a molecule (e.g., Gao and Marcus 2002). These values are for 140 K.
[3] Gao and Marcus (2002).

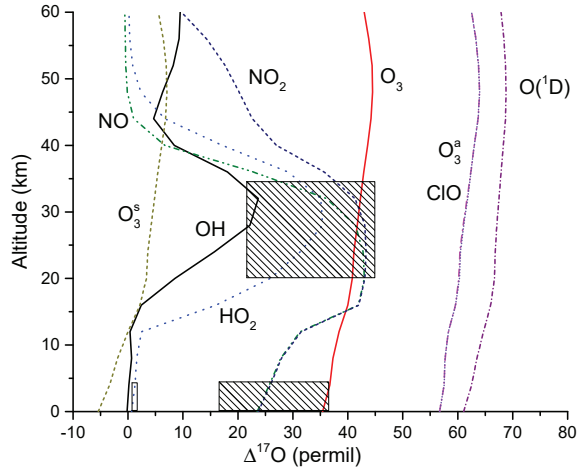

Figure 1. Photochemical equilibrium model results. Calculations assume an O atom exchange rate coefficient of 1×10^{-19} cm^3 s^{-1} between OH and O_2, well below the upper limit value (Table 2). The **hatched regions** show the range of $\Delta^{17}O$ measurements for stratospheric (Schueler et al. 1990; Krankowsky et al. 2000) and tropospheric (Krankowsky et al. 1995; Johnston and Thiemens 1997) O_3. The **narrow rectangle** near the origin is the range of measurements in rainwater H_2O_2 (Savarino and Thiemens 1999). This figure closely follows Lyons (2001) but with an updated isotopic branching ratios (see text), with a non-zero exchange rate for OH and O_2, and with the addition of symmetric ozone. Slope = 0.520

Figure 1 includes exchange reactions (X1–X7), and (X9) (Table 2), with the rate coefficient for X6 set arbitrarily to 1×10^{-19} cm^3 s^{-1}. If the rate coefficient for X6 is set to zero (as in Fig. 1 of Lyons 2001), the maximum $\Delta^{17}O$ values for OH are about 27‰ from 28–32 km, several permil higher than shown here, but still about 20‰ lower than Figure 1 in Lyons (2001). Using the improved isotopic branching ratios has a quantitative impact on atmospheric $\Delta^{17}O$ values, but does not change the qualitative picture of the prediction of an enrichment of ^{17}O in many stratospheric species (Lyons 2001). It is also possible that additional O exchange reactions are present, which will further modify the $\Delta^{17}O$ values shown in Figure 1. Exchange reactions for ClO have not been included here.

Table 2. O atom exchange rate coefficients (Lyons 2001).

	Reaction	Rate coefficient cm^3s^{-1}	Ref.
X1	$O + O \leftrightarrow OO + O$	2.9(–12)	a
X2	$Q + NO \leftrightarrow O + NQ$	3.7 (–11)	a
X3	$QH + H_2O \leftrightarrow OH + H_2Q$	2.3 (–13)$e^{-2100/T}$	b
X4	$QH + NO \leftrightarrow OH + NQ$	1.8 (–11)	c
X5	$QH + NO_2 \leftrightarrow OH + NOQ$	1.0 (–11)	c
X6	$QH + O_2 \leftrightarrow OH + OQ$	<1 (–17)	c
X7	$QH + HO_2 \leftrightarrow OH + HQO$	1.7 (–11) $e^{400/T}$	d
X8	$HOQ + O_2 \leftrightarrow HO_2 + OQ$	<3 (–17)	e
X9	$NQ + NO_2 \leftrightarrow NOQ + NO$	3.6 (–14)	f
X10	$NOQ + O_2 \leftrightarrow NO_2 + OQ$	<1 (–24)	g
X11	$NOQ + H_2O \leftrightarrow NO_2 + H_2Q$	rapid (?)	h
X12	$QH + CO \leftrightarrow OH + CQ$	<1 (–15)	c
X13	$QH + CO_2 \leftrightarrow OH + COQ$	<1 (–17)	c

References: a. Anderson et al. (1985); b. Dubey et al. (1997); c. Greenblatt and Howard (1989); d. Dransfield and Wagner (1987); e Sinha et al. (1987); f Klein et al. (1963); g Sharma et al. (!970); h Jaffe and Klein (1966)

Ab initio calculations from Francisco (1998) predict a 3.1 kcal mol^{-1} barrier above the bond dissociation energy of the HOClO adduct. At stratospheric temperatures this barrier (1560 K) implies a relatively slow rate of exchange with OH, but other exchange reactions could be important, although exchange with O_2 is unlikely.

Figure 2 shows $\Delta^{17}O$ values from the Lyons (2001) model, but that have not been previously published. The CO_2 are not computed here, but instead are specified from Lämmerzahl et al. (2002).

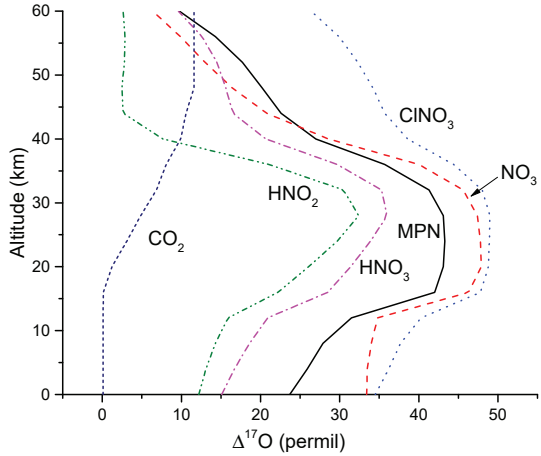

Figure 2. $\Delta^{17}O$ values for several other species included in the Lyons (2001) model, but not previously shown. The CO_2 values are specified (Lämmerzahl et al. 2002), whereas the others are computed. MPN is methyl peroxy nitrate ($CH_3O_2NO_2$). These values are more qualitative than quantitative. For example, we have not considered exchange reactions for any of the computed species. Slope = 0.520.

'MPN' is methyl peroxy nitrate, $CH_3O_2NO_2$, and is meant to be representative of the class of peroxy nitrate compounds. A more complete analysis of the $\Delta^{17}O$ of nitric acid and precursor nitrates is given in Michalski et al. (2004). Exchange reactions have not been included for any of these species. Far more complete models now exist, especially for the nitrates, as will be discussed further below.

Turning next to O_3 isotopic models, detailed modeling of stratospheric ozone isotopes was presented in Liang et al. (2006). Isotope fractionation due to ozone formation reactions were carefully modeled using the results of the semi-empirical model of Gao and Marcus (2002) and the laboratory measurements of Morton et al. (1990). Fractionation associated with ozone photolysis was also accounted for. The model reproduced balloon-borne mass spectrometer measurements from 20–35 km quite well (Liang et al. 2006). More recently Young et al. (2014) have argued that including the mass-dependence of kinetic rate coefficients in ozone formation reactions has a non-negligible effect on the MIF signatures of the resulting O_3. As has been discussed previously in Lyons (2001), in a hard-sphere approximation, a gas-phase bimolecular rate coefficient may be expressed in the form $k \sim \sigma_c v_{th} e^{-E_a/kT}$ where σ_c is the collision cross section, v_{th} is the thermal velocity, and E_a is the activation energy. The thermal velocity is $v_{th} \propto 1/\sqrt{u}$ where μ is the reduced mass of the reactants. Young et al. (2014) showed that inclusion of even this simple reduced mass factor reduces the MIF signatures of O_3 products, producing better agreement with measurements. Most of the models results described here (Lyons 2001 included) have not accounted for the reduced mass in the isotopic rate coefficients.

Trace but measurable $\Delta^{17}O$ signatures were predicted for tropospheric CO_2 (Hoag et al. 2005). In the stratosphere CO_2 acquires a large MIF signature due to exchange with $O(^1D)$(Yung al. 1991). In the troposphere CO_2 exchanges O primarily with biospheric water. Using a two-box model, and accounting for the rates of exchange in the biosphere and the flux of CO_2 from the stratosphere, Hoag et al. (2005) predict $\Delta^{17}O = 0.13$ and 0.15‰ (VSMOW, slope $\lambda = 0.516$) for the northern and southern hemispheres, respectively (Fig. 3). These results mean that $\Delta^{17}O$ can be used as an additional tracer of biospheric productivity, and of the rate of exchange of stratospheric and tropospheric air, as has been done for O_2 (e.g., Bender et al. 1994).

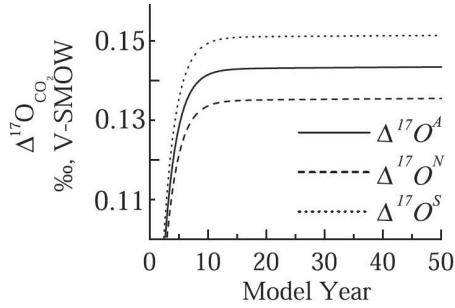

Figure 3. Box model prediction of $\Delta^{17}O$ for tropospheric CO_2 for the global average (**solid line**), the northern hemisphere (**dashed**), and the southern hemisphere (**dotted**). (Figure from Hoag et al. (2005), Geophys. Res. Lett. 32, L02802.)

The predictions of Hoag et al. (2005) have been confirmed by measurements in Taiwan (Mahata et al. 2016), and by measurements and modeling in the vicinity of Göttingen, Germany (Hofmann et al. 2017). 3D modeling also demonstrates this MIF signature in atmospheric CO_2 on a fairly well-resolved grid (Fig. 4), although with MIF signatures lower than the Hoag et al. (2005) model. All of these results confirm that $\Delta^{17}O$ of CO_2 can be used as a tracer of C in the atmosphere. As an example of this, Liang and Mahata (2015) used an enhanced $\Delta^{17}O$ in surface CO_2 to infer intrusion of stratospheric air, possibly associated with tropopause folding.

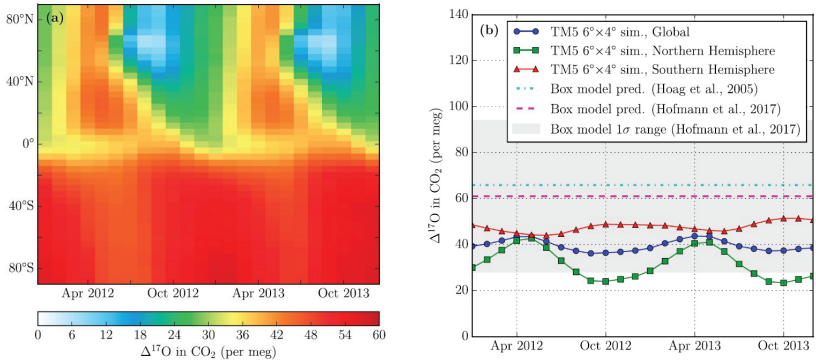

Figure 4. Monthly average of simulated $\Delta^{17}O$ using a 3D model (TM5) with a 6°×4° horizontal resolution and 25 vertical levels. **(a)** Heat diagram for $\Delta^{17}O$, with values are expressed in per meg rather than per mil. **(b)** Comparison with previously published box models. (Figure from Koren et al. (2019) *J Geophys Res Atmos* 124:8808–8836.)

Stratospheric CO_2 exhibits a slope ~1.6–1.7 on a 3-oxygen isotope plot ($\delta^{17}O$ vs. $\delta^{18}O$) discovered by balloon measurements from Lämmerzahl et al. (2002). Such a high slope in excess of 1 arises from exchange of CO_2 with $O(^1D)$ released by O_3 photolysis (Yung et al. 1991; Liang et al. 2007). Clumped isotope work on stratospheric CO_2, in particular, measurement of $^{16}O^{13}C^{18}O$ (mass 47) from stratospheric air samples, has revealed a large meridional variation in mass 47 (Yeung et al. 2009). The mid-latitude mass 47 abundances are consistent with exchange of CO_2 with $O(^1D)$, but polar vortex abundances indicate another fractionation process at work, possible temperature dependent exchange on polar stratospheric clouds particles.

Next, we consider the MIF signature of stratospheric water. A prediction from Lyons (2001) was that stratospheric water could have a positive $\Delta^{17}O$ value, because $O(^1D)$ produced by photolysis of one of the terminal O atoms on O_3 produces OH upon reaction with stratospheric H_2O. Formation of stratospheric H_2O occurs by the oxidation of CH_4 by OH. A more detailed analysis of this possibility by Zahn et al. (2006) using a 1-D photochemical model showed that stratospheric OH could have $\Delta^{17}O$ ~ +30‰ near 30 km (Fig. 5a), leading to stratospheric H_2O with $\Delta^{17}O$ ~ +10‰. These values are slightly in error because Zahn et al. (2006) assumed that symmetric O_3 has $\Delta^{17}O$ ~ +25‰, rather than closer to 0‰, as discussed above. Again, the results are dependent on several uncertain rate coefficients for O atom exchange. Zahn et al. (2006) also present $\delta^{18}O$ values (Fig. 5b), but these results do not include the reduced mass scaling of the isotopic rate coefficients. Measurements of water vapor samples from the Arctic (Alert, Canada) and Antarctica (Vostok) by Lin et al. (2013) and Winkler et al. (2013), respectively, have demonstrated a component of ^{17}O-enriched water from the stratosphere as a result of the overall Brewer-Dobson meridional circulation. Direct sampling of water vapor in the upper troposphere and lower stratosphere yielded $\Delta^{17}O$ ~ 0‰ with uncertainty of about 2‰, but it was not entirely clear from where the sampled air was originating (Franz and Röckmann 2005).

Turning next to nitrates, Michalski et al. (2003, 2004) identified the key nitrate $\Delta^{17}O$ formation pathways and used $\Delta^{17}O$ signatures to definitely show that the Atacama nitrates are mostly atmospherically derived. In a time-dependent study, diurnal variation of $\Delta^{17}O$ of nitrate was simulated using an atmospheric chemistry box model for HO_x, NO_x, and NO_y species (Morin et al. 2011). Because of the strong diurnal variation in the chemistry of nitrate formation, and in the NO_x and NO_y precursors, quite large diurnal variations in $\Delta^{17}O$ were predicted (Fig. 6). For NO_2, the minimum in $\Delta^{17}O$ ~ 28‰ and occurred near local noon, while the maximum ~ 38–40‰ and occurred at night (Morin et al. 2011). Similar variations,

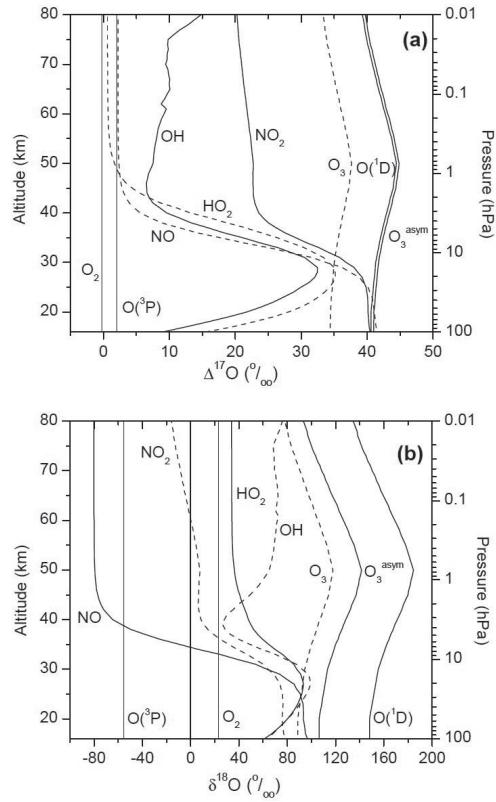

Figure 5. 1-D photochemical simulation of the oxygen isotopes of several radical species in the atmosphere. These results assume $\Delta^{17}O = +25‰$ for symmetric O_3, which implies $\Delta^{17}O$ values for asymmetric O_3 that are too low. A positive MIF signature for stratospheric OH is predicted. (Figure from Zahn et al. (2006), Atmos. Chem. Phys. 6: 2073–2090).

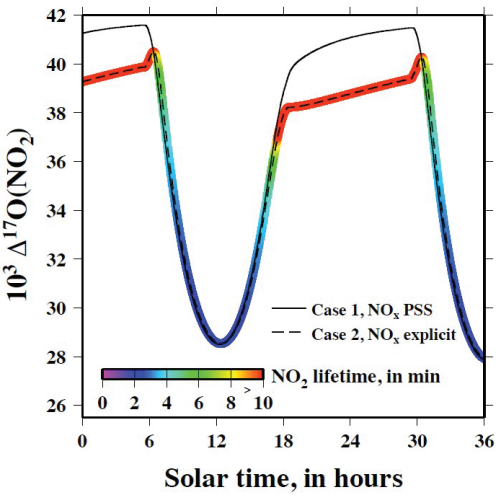

Figure 6. Diurnal variation of $\Delta^{17}O$ of NO_2 for two cases. Case 1 assumes photochemical steady state (PSS), and Case 2 is an explicit kinetic calculation. The NO_2 photolytic lifetime is shown by the overlain color. (Figure from Morin et al. (2011) Atmos. Chem. Phys. 11: 3653–3671)

although for smaller mean $\Delta^{17}O$ values, were found for HO_2 and H_2O_2. Global simulations of nitrate with a 1 km cloud model, with highly detailed chemical pathways, reveal large geographical variations in $\Delta^{17}O$ (Alexander et al. 2020). Over Amazonia, the dominance of $RONO_2$ hydrolysis yields mean values of just 3–4‰, whereas over the mid-latitude oceans, the dominance of XNO_3 hydrolysis (X = halogen atom) yields mean values over 30‰ (Fig. 7).

On the topic of MIF signatures in sulfates, a key driver has been the transfer of $\Delta^{17}O$ to sulfate during the oxidation of volcanic plume SO_2. There are many oxidation pathways for SO_2 in the modern atmosphere including by O_3, by H_2O_2, and by O_2, depending on the pH of the participating aerosol. Although our emphasis thus far has been on the modern Earth atmosphere (Martin et al. 2014), several major eruptions have occurred since the Pleistocene that have left well known tuff formations, including the Lara Creek Tuff (LCT, 0.64 Ma), the Huckleberry Ridge Tuff (HRT, 2.04 Ma), and the Bishop Tuff (0.76 Ma). Analysis of the O isotope composition of sulfate in these tuffs yielded constraints on total O_3 consumed by the corresponding volcanic eruption (Fig. 8) (Martin and Bindeman 2009).

Another key application of sulfate MIF signatures has been to elucidate oxidation mechanisms. Alexander et al. (2011) used observations of $\Delta^{17}O$ in non-sea-salt sulfate to quantify the formation pathways in marine boundary layer sulfate. For their northeast Atlantic ocean collection site, they determined that oxidation of S(IV) by O_3 accounted for about 36% of in-cloud sulfate formation. Similarly, but in a different context, $\Delta^{17}O$ of Antarctic ice core sulfates and nitrates have been used to infer changes in oxidation mechanisms in the southern hemisphere since the 19th century. The observed increase in $\Delta^{17}O$ of sulfates is consistent with greater oxidation by O_3, and the observed decrease in $\Delta^{17}O$ of nitrates is interpreted to be due an increase in RO_2 over O_3 in NO_x cycling (Sofen et al. 2014). More recently, Lin et al. (2017) used $\Delta^{17}O$ and ^{35}S (a radiogenic isotope) in sulfates collected in eastern China to determine that the formation pathway for tropospheric sulfate is vertically uniform, likely due to strong convection in this region.

Finally, we also consider applications of MIF signatures to atmospheric pollution, particularly urban environments. Li et al. (2013) analyzed a long record of sulfates collected in

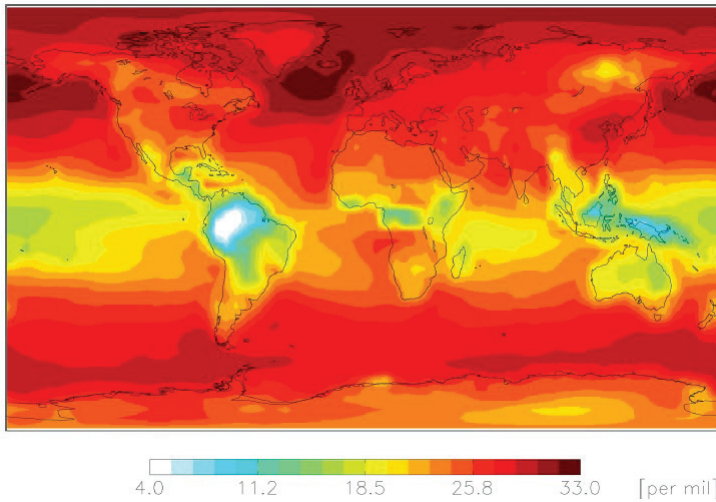

Figure 7. Simulation of annual mean global nitrate $\Delta^{17}O$ values for a 1 km cloud model. The wide range in nitrate MIF signature results from the relative importance of XNO_3 hydrolysis (high $\Delta^{17}O$) and $RONO_2$ hydrolysis (low values). (Figure from Alexander et al. (2020) Atmos Chem Phys 20:3859–3877).

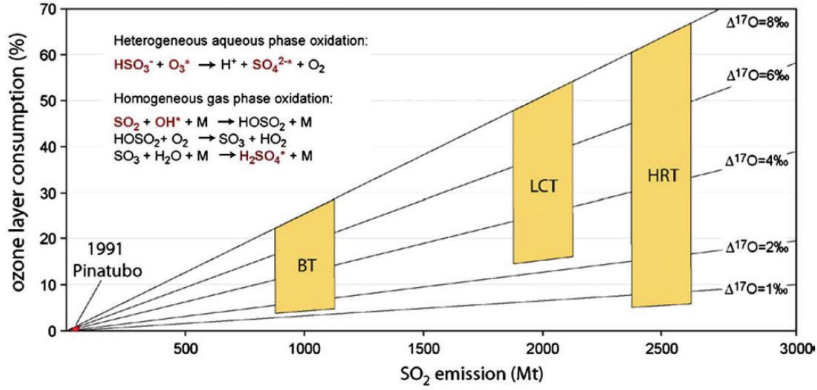

Figure 8. Estimates of ozone layer consumption from several large volcanic eruptions in California dry lake beds over the past 2 Ma. BT, LCT, and HRT are defined in the text. Several important SO_2 oxidation mechanisms are shown. (Figure reprinted with permission of Elsevier from Martin E, Bindeman I (2009) Mass-independent isotopic signatures of volcanic sulfate from three supereruption ash deposits in Lake Tecopa, California. Earth Planet Sci Lett 282:102–114.)

Wuhan and found $\Delta^{17}O \sim 0.6‰$, similar to Baton Rouge, Louisiana. The similarity is surprising given the difference in rainwater pH in the two locations, which leads Li et al to suggest that S(IV) oxidation by metals is more important in the dust-rich Wuhan atmosphere. Laskar et al. (2020) have used $\Delta^{17}O$ of CO_2 air in Delhi, India to distinguish between the fossil fuel and rice straw burning contribution. Combined with a mixing model, they have determined that rice straw burning contributes ~70% to anthropogenic CO_2.

RESULTS FOR THE UPPER ATMOSPHERE

The isotopic composition of Earth's upper atmosphere (above 100 km) has not received much attention. The lower atmosphere is mostly well-mixed due to the motions of turbulent eddies and breaking atmospheric waves. In photochemical models, eddy transport is approximated as a diffusive process, and is referred to as eddy diffusion. Compositionally, the upper atmosphere above the homopause, the upper boundary of the well-mixed atmosphere at ~ 100km, is dominated by O atoms, and transport by molecular diffusion dominates over eddy diffusion. Considering these conditions, we present simulations of the O isotope composition of O atoms in the thermosphere up to escape altitudes (~ 500 km).

The thermosphere represents the transition from convective and radiative energy transport below the homopause to primarily conductive energy transport above the homopause (Chamberlain and Hunten 1990). Generation of hot O atoms due to far-UV and extreme-UV heating of O_2 and N_2 in the ionosphere creates the high temperatures (~ 1000 K) from which the thermosphere's name originally derived. Below the homopause, isotope fractionation results from photochemical reactions (mostly mass-dependent), non-statistical photochemistry, such as for O_3 (mostly mass-independent), or from condensation/evaporation processes (mass-dependent). Eddy mixing below the homopause keeps transport-derived isotope fractionation to a minimum. Above the homopause, molecular diffusion dominates transport, and massive mass-dependent fractionation results.

For the thermosphere, diffusive equilibrium (i.e., zero flux) conditions are informative. Setting $f_i = 0$ in Equation (2), and solving for n_i, we find

$$n_i(z) = n_i(z_0)\exp\left(-\int_{z_0}^{z}\left(\frac{D_i}{H_i}+\frac{K}{H_a}\right)\frac{1}{D_i+K}dz\right) \tag{16}$$

where z_0 is a reference height, which could be the ground, the homopause, or some other preferred height (Banks and Kockarts 1973). We will use Equation (16) to get a sense of the expected isotope fractionation in the thermosphere, and compare those results to a photochemical simulation using the VULCAN model (Tsai et al. 2017).

We first ran VULCAN to simulate Earth's atmosphere from the ground up to 500 km, the approximate upper boundary of the atmosphere for which the mean free path of an atom is comparable to its scale height. This height varies with the solar cycle up to a maximum of about 1000 km for peak solar activity. Our VULCAN runs included the minor isotopes of oxygen (^{17}O and ^{18}O), but did not include the non-statistical rate constants of O_3 formation (Hathorn and Marcus 2000; Gao and Marcus 2002), which is the primary source of mass-independent fractionation in the atmosphere below the homopause (e.g., Thiemens and Heidenreich 1983, Lyons 2001). The temperature and pressure profiles are from the US standard atmosphere model (e.g., Chamberlain and Hunten 1990). The corresponding ion and electron number density profiles were also computed. These non-isotopic number density profiles are not shown here, but will be presented elsewhere. The ion species do not include water cluster positive ions or negative ions (e.g., Brasseur and Solomon 1984), corresponding to the D-layer of the ionopshere.

We focus on O atoms calculated from both diffusion theory (Eqn. 16) and from the full VULCAN photochemical model of the upper atmosphere. Figure 9 shows the number densities for the stable oxygen isotopes calculated by these two methods. The solid lines are the results from the diffusion theory equations for an assumed isothermal temperature of 500 K, and the dashed lines are the VULCAN full kinetic results. The number density (in cm^{-3}) for ^{16}O is in blue, ^{17}O is in green, and ^{18}O is in red. We expect to see the slope of the number density lines to be different below and above the homopause, due to diffusive separation. The isothermal diffusion theory approximation has a slope change at around 200 km. This height differs significantly from the true Earth homopause because Earth's atmospheric temperature profile is not isothermal, but instead varies from about 200 to 1000 K. The VULCAN results diffusively separate near 100 km, closer to the true Earth homopause.

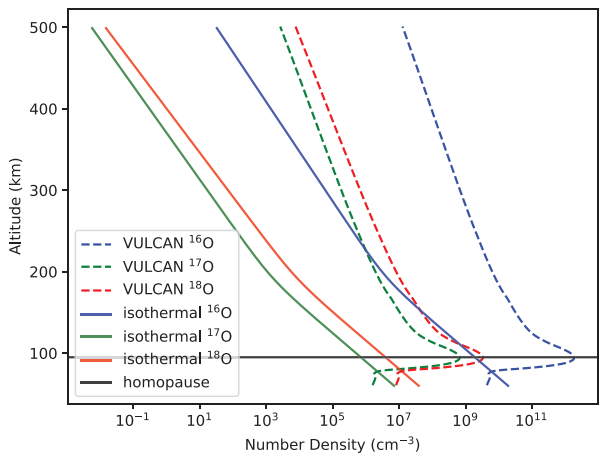

Figure 9. The number densities for the stable oxygen isotopes of O atoms, calculated from diffusion theory for a 500 K isothermal atmosphere (**solid lines**) and using VULCAN (**dashed lines**). The true homopause is shown with the **solid black line**. (Brinjikji and Lyons 2020a).

The delta-values for thermospheric O atoms are shown in Figure 10. The values for $\delta^{17}O$ and $\delta^{18}O$ (‰) calculated are shown for diffusion theory (solid lines) and VULCAN photochemical modeling (dashed lines). The delta values from the diffusion theory approximation are depleted by about −100‰ more than the VULCAN results for both $\delta^{17}O$ and $\delta^{18}O$ above about 400 km. Both models show evidence of diffusive separation above the homopause. As in Figure 9, the diffusion theory model is for an isothermal atmosphere that does not have the correct location of the homopause, yet the isotope fractionation is qualitatively similar to that obtained with VULCAN.

The $\Delta^{17}O$ for these two cases is shown in Figure 11 with from diffusion theory shown as solid lines and from VULCAN shown as dashed lines. However, the slope factor of 0.528 results in enrichments on the order of 40‰ near the exobase (Figure 11). Based on the barometric law behavior of the individual isotopes undergoing molecular diffusion, we redefined $\Delta^{17}O$ to have slope $\lambda = 0.500$ which results in a depletion of −2‰ from the diffusion theory calculation and an enrichment of 5‰ from VULCAN (Fig. 11). We have not yet determined the source of these still very large values, but it's clear that a fractionation law using 0.528 or 0.52 is not correct in the thermosphere.

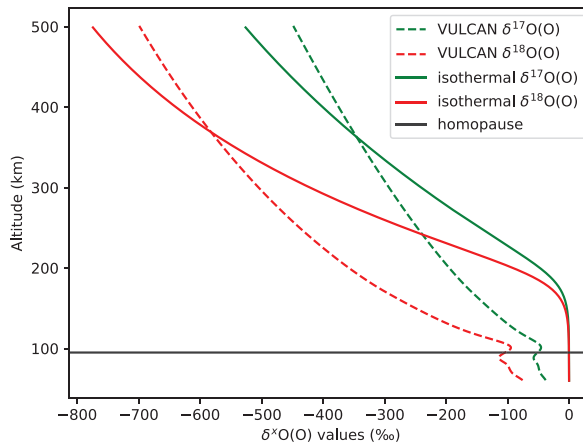

Figure 10. The delta values (‰) for and calculated from isothermal diffusion theory (**solid lines**) and using VULCAN (**dashed lines**). The homopause is shown with the **solid black line**.

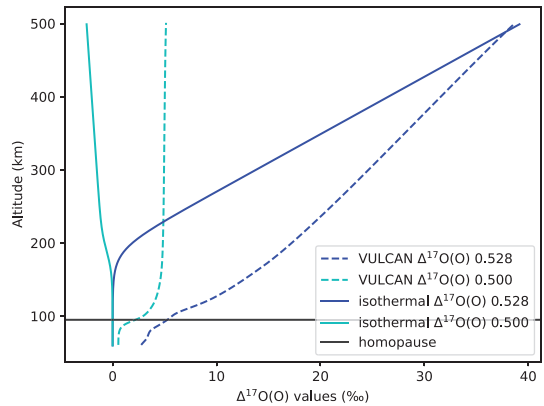

Figure 11. The values for thermospheric O atoms calculated from isothermal diffusion theory (**solid lines**) and using VULCAN (**dashed lines**). (Brinjikji and Lyons 2020a).

DISCUSSION

Improvements in the accuracy and interpretation of $\Delta^{17}O$ modeling in the well-mixed atmosphere (below 100 km) will come from two key areas. First, a complete accounting of mass-dependent effects in the kinetics. Young et al. (2014) make this point for O_3 formation, but this will extend to most of the other species isotopically influenced by O_3. Second, the data on exchange reactions is still incomplete, especially for gas phase exchange. Several of the exchange reactions in Table 2 have rather high upper limits to their rate coefficients. Laboratory measurements could provide much tighter constraints on these rate coefficients, which would significantly improve the accuracy of isotopic model predictions.

For the upper atmosphere, we focus discussion on diffusive separation of isotopes. To illustrate why a 0.50 fractionation law better describes mass-dependent isotope fractionation in the thermosphere (Fig. 11), we consider number density profiles for O atoms well above the homopause. This ensures that only molecular diffusion is affecting isotope ratios. For diffusive equilibrium in an isothermal atmosphere, the number density profile is given by

$$n_i(z) = n_i(z_h)\mathrm{e}^{-(z-z_h)/H_i} \tag{17}$$

where z_h is the height of the homopause. Using the ratios of number densities to compute delta-values relative to the homopause, we have

$$\frac{n_x(z)}{n_{16}(z)} = \frac{n_x(z_h)}{n_{16}(z_h)}\mathrm{e}^{-(z-z_h)\left(\frac{1}{H_x}-\frac{1}{H_{16}}\right)} \tag{18}$$

where the difference of the inverse scale heights is

$$\frac{1}{H_x} - \frac{1}{H_{16}} = \frac{g}{\mathrm{k}T}(m_x - m_{16}) \tag{19}$$

The corresponding delta-values are $\delta^x\mathrm{O} = \frac{n_x}{n_{16}} - 1.$. For small arguments in the exponential of Equation (18), the delta-values become

$$\delta^x\mathrm{O} \approx -(z - z_h)\frac{g}{\mathrm{k}T}(m_x - m_{16}) \tag{20}$$

From equation 20, the linear dependence on mass difference means that $\delta^{17}O/\delta^{18}O \approx 0.50$. This continues to be largely true for the full exponential form of Equation (18) as well. The barometric law behavior of gases in diffusive equilibrium in an atmosphere yields mass-dependent behavior, but with a fractionation law exponent that differs fundamentally from the more usual 0.52–0.53 law that results from either zero-point energy, vibrational partition function, or collisional mass dependence (Bigeleisen 1965; Matsuhisa et al. 1977; Weston 1999; Young et al. 2000).

CONCLUSIONS

We have reviewed model results for the mass-independent fractionation of O isotopes in the lower atmosphere. We presented updated results from Lyons (2001), together with later modeling of $\Delta^{17}O$ of stratospheric H_2O from Zahn et al. (2006). A definitive measurement confirming a MIF signature (possibly as high as 10‰) in stratospheric water has yet to be made, but there are strong suggestions of MIF stratospheric water in Arctic and Antarctic tropospheric water samples (Lin et al. 2013; Winkler et al. 2013). The small MIF signature ($\Delta^{17}O \sim 0.1$‰) of tropospheric CO_2 has been shown to be an effective tracer of C in the lower atmosphere in a 2-box model (Hoag et al. 2005) and in a global 3D model (Koren et al. 2019).

Recent work on global 3D modeling of $\Delta^{17}O$ of nitrates demonstrates the importance of the MIF carrier, with XNO_3 hydrolysis producing large signatures ($\Delta^{17}O$ ~30‰) versus $RONO_2$ hydrolysis (e.g., over Amazonia) yielding dramatically smaller MIF signatures ($\Delta^{17}O$ ~3‰) (Alexander et al. 2020). MIF signatures of sulfate formation have been used to elucidate the complex oxidation pathways for S(IV) in various environments (e.g., Alexander et al. 2005), and to estimate ozone layer consumption from large volcanic eruptions (Martin and Bindeman 2009). A theme that emerges from these studies is the impressive diversity of applications of O MIF signatures in the atmosphere. It is important to remember that the models may be limited by the available data, particularly with respect to poorly constrained rate coefficients for exchange reactions. In addition, the models need to properly account for mass-dependent fraction of O isotopes, by, at the very least, including the reduced mass in isotopic rate coefficients.

We have also presented new results of a model analysis of O isotope fractionation in the upper atmosphere, specifically above the homopause (~ 100 km). Diffusive separation of isotopes is the predominant feature, with massive (several 100's of permil) depletion of ^{17}O and ^{18}O relative to ^{16}O for atomic oxygen, the primary component of the upper atmosphere. Preliminary supporting evidence for such massive fractionation comes from measurements of Al samples from the Long Duration Exposure Facility (LDEF), which sampled the atmosphere at altitudes from 470 to 340 km over a 6 year period (Brinjikji and Lyons 2020b). In an additional modeling result, we found that the mass-dependent fractionation that accompanies diffusive separation has a fractionation law exponent closer 0.50 than to the more usual values of 0.52–0.53 (Brinjikji and Lyons 2020a). This derives from the difference in scale heights in the barometric laws that describe atoms in the thermosphere.

In summary, our main conclusions are as follows.

1. Improved laboratory rate coefficients for exchange reactions are needed for models of MIF signatures in the lower atmosphere (below 100 km). Also, a more careful accounting of mass-dependent fractionation should improve the accuracy of model computed MIF signatures.
2. In the upper atmosphere (> 100 km), diffusive separation due to molecular diffusion of the isotopes of atomic oxygen leads to massive depletions (by 100's ‰) of ^{17}O and ^{18}O by altitudes approaching the exobase (~ 500 km). 3) Diffusive separation is a type of mass-dependent fractionation, but it exhibits a slope (λ) closer to 0.50 than to the more usual mass-dependent fractionation slopes of 0.52–0.53.

ACKNOWLEDGEMENTS

The authors gratefully acknowledge numerous discussions with Shang-Min Tsai on the use of the VULCAN photochemical code, and on python in general. JRL acknowledges support from the NASA LARS program (grant #80NSSC18K0841 to ASU).

REFERENCES

Alexander B, Park RJ, Jacob DJ, Li QB, Yantosca RM, Savarino J, Lee CCW, Thiemens MH (2005) Sulfate formation in sea-salt aerosols: Constraints from oxygen isotopes. J Geophys Res Atmos 110:1–12

Alexander B, Allman DJ, Amos HM, Fairlie TD, Dachs J, Hegg DA, Sletten RS (2011) Isotopic constraints on the formation pathways of sulfate aerosol in the marine boundary layer of the subtropical northeast Atlantic Ocean. J Geophys Res 117:D06304

Alexander B, Sherwen T, Holmes CD, Fisher JA, Chen Q, Evans MJ, Kasibhatla P (2020) Global inorganic nitrate production mechanisms: comparison of a global model with nitrate isotope observations. Atmos Chem Phys 20:3859–3877

Anderson SM, Klein FS, Kaufman F (1985) Kinetics of the isotope exchange reaction of ^{18}O with NO and O_2 at 298 K. J Chem Phys 83:1648–1656

Bao H, Campbell DA, Bockheim JG, Thiemens MH (2000) Origins of sulphate in Antarctic dry-valley soils as deduced from anomalous ^{17}O compositions. Nature 407:499–502

Bao H, Michalski GM, Thiemens MH (2001) Sulfate oxygen−17 anomalies in desert varnishes. Geochim Cosmochim Acta 65:2029–2036

Bao, H, Lyons JR, Zhou C (2008) Triple oxygen isotope evidence for elevated CO_2 levels after a Neoproterozoic glaciation. Nature 453:504–506

Banks PM, Kockarts G (1973). Aeronomy, Part B. Academic Press, New York

Bender ML, Sowers T, Labeyrie L (1994) The Dole effect and its variations during the last 130,000 years as measured in the Vostok ice core. Global Biogeochem Cycles 8:363–376

Bigeleisen J (1965) Chemistry of isotopes. Science 147:463–471

Brasseur G, Solomon S (1984) Aeronomy of the Middle Atmosphere, D. Reidel, Dordrecht

Brinjikji M, Lyons JR (2020a) The effects of diffusion on oxygen isotopes in earth's upper atmosphere. LPSC abstract #2317

Brinjikji M, Lyons JR (2020b) Oxygen isotope fractionation in earth's upper atmosphere. LPSC abstract #2322

Chamberlain R, Hunten D (1990) The Theory of Planetary Atmospheres, An Introduction to their Physics and Chemistry (2nd Ed). Academic Press, New York

Dransfield P, Wagner HG (1987) Comparative study of the reactions of ^{16}OH and ^{18}OH with $H^{16}O_2$. Z Naturforsch 42a:471–476

Dubey MK, Mohrschladt R, Donahue NM, Anderson JG (1997) Isotope specific kinetics of hydroxyl radical (OH) with water (H_2O): testing models of reactivity and atmospheric fractionation. J Phys Chem A 101:1494:1500

Francisco JS (1998) Oxygen atom exchange in reactions of OH radicals with NO and ClO. Chem Phys Lett 285:138–142

Franz P, Röckmann T (2005) High-precision isotope measurements of $H_2{}^{16}O$, $H_2{}^{17}O$, $H_2{}^{18}O$, and the $\Delta^{17}O$-anomaly of water vapor in the southern lowermost stratosphere. Atmos Chem Phys 5:2949–2959

Gao YQ, Marcus RA (2002) On the theory of the strange and unconventional isotopic effects in ozone formation. J Chem Phys 116:137–154

Gautier E, Savarino J, Hoek J, Erbland J, Caillon N, Hattori S, Yoshida N, Albalat E, Albarede F, Farquhar J (2019) 2600-years of stratospheric volcanism through sulfate isotopes. Nat Comm 10:1–7

Greenblatt GD, Howard CJ (1989) Oxygen atom exchange in the interaction of ^{18}OH with several small molecules. J Phys Chem 93:1035–1042

Hathorn BC, Marcus RA (2000) An intramolecular theory of the mass-independent isotope effect for ozone: II. Numerical implementation at low pressures using a loose transition state. J Chem Phys 113:9497–9509

Hoag KJ, Still CJ, Fung IY, Boering KA (2005) Triple oxygen isotope composition of tropospheric carbon dioxide as a tracer of terrestrial gross carbon fluxes. Geophys Res Lett 32:L02802

Hodgskiss MSW, Crockford PW, Peng Y, Wing BA, Horner TJ (2019) A productivity collapse to end Earth's Great Oxidation. PNAS 116:17208–17212

Hofmann MEG, Horváth B, Schneider L, Peters W, Schützenmeister K, Pack A (2017) Atmospheric measurements of $\Delta^{17}O$ in CO_2 in Göttingen, Germany reveal a seasonal cycle driven by biospheric uptake. Geochim Cosmochim Acta 199:143–163

Jaffe S, Klein FS (1966) Isotopic exchange reactions atomic oxygen produced by the photolysis of NO_2 at 3660 Å. Far Soc Trans 62:3135:3141

Jakosky BM, Jones JH (1994) Evolution of water on Mars. Nature 370 :328–329

Jakosky BM, Slipski M, Benna M, Mahaffy P, Elrod M, Yelle R, Stone S, Alsaeed N (2017) Mars' atmospheric history derived from upper-atmosphere measurements of Ar−38/Ar−36. Science 355:1408

Jakosky BM, Brain D, Chaffin M, Curry S, Deighan J, Grebowsky J, Halekas J, Leblanc F, Lillis R, Luhmann JG, Andersson L (2018) Loss of the Martian atmosphere to space: Present-day loss rates determined from MAVEN observations and integrated loss through time. Icarus 315:146–157

Janssen C, Guenther J, Krankowsky D, Mauersberger K (1999) Relative formation rates of $^{50}O_3$ and $^{52}O_3$ in ^{16}O–^{18}O mixtures. J Chem Phys 111:7179–7182

Johnston GC, Thiemens MH (1997) The isotopic composition of tropospheric ozone in three environments. J Geophys Res 102:25395–25404

Klein FS, Spindel W, Stern MJ (1963) Catalysis of isotopic exchange in nitric oxide. J Chim Phys 60:148–153

Koren G, Schneider L, van der Velde IR, van Schaik E, Gromov SS, Adnew GA, Mrozek Martino DJ, Hofmann ME, Liang MC, Mahata S, Bergamaschi P (2019) Global 3-D simulations of the triple oxygen isotope signature $\Delta^{17}O$ in atmospheric CO_2. J Geophys Res Atmos 124:8808–8836

Krankowsky D, Bartecki F, Klees GG, Mauersberger K, Schellenbach K, Stehr J (1995) Measurement of heavy isotope enrichment in tropospheric ozone. Geophys Res Lett 22:1713–1716

Krankowsky D, Lämmerzahl P, Mauersberger K (2000) Isotopic measurements of stratospheric ozone. Geophys Res Lett 27:2593–2595

Lämmerzahl P, Röckmann T, Brenninkmeijer CAM, Krankowsky D, Mauersberger K (2002) Oxygen isotope composition of stratospheric carbon dioxide. Geophys Res Lett 29:1582

Laskar AH, Maurya AS, Singh V, Gurjar BR, Liang M-C (2020) A new perspective of probing the level of pollution in the megacity Delhi affected by crop residue burning using the triple oxygen isotope technique in atmospheric CO_2. Environ Pollution 263:114542

Li X, Bao H, Gan Y, Zhou A, Liu Y (2013) Multiple oxygen and sulfur isotope compositions of secondary atmospheric sulfate in a mega-city in central China. Atmos Environ 81:591–599

Liang M-C, Mahata S (2015) Oxygen anomaly in near surface carbon dioxide reveals deep stratospheric intrusion. Sci Rep 5:11352

Liang M-C, Irion FW, Weibel JD, Miller CE, Blake GA, Yung YL (2006) Isotopic composition of stratospheric ozone. J Geophys Res 111:2302–2313

Liang M-C, Blake GA, Lewis BR, Yung YL (2007) Oxygen isotopic composition of carbon dioxide in the middle atmosphere. PNAS 104:21–25

Lin Y, Clayton RN, Huang L, Nakamura N, Lyons JR (2013) Oxygen isotope anomaly observed in water vapor from Alert, Canada and the implication for the stratosphere. PNAS 110:15608–15613

Lin M, Biglari S, Zhang Z, Crocker D, Tao J, Su B, Liu L, Thiemens MH (2017) Vertically uniform formation pathways of tropospheric sulfate aerosols in East China detected from triple stable oxygen and radiogenic sulfur isotopes. Geophys Res Lett 44:5187–5196

Luz B, Barkan E, Bender ML, Thiemens MH, Boering KA (1999) Triple-isotope composition of atmospheric oxygen as a tracer of biospheric productivity. Nature 400:547–550

Lyons JR (2001) Transfer of mass-independent fractionation in ozone to other oxygen-containing radicals in the atmosphere. Geophys Res Lett 28:3231–3234

Mahata S, Wang C-H, Bhattacharya SK, Liang M-C (2016) Near surface CO_2 triple oxygen isotope composition. Terr Atmos Ocean Sci 27:99–106

Martin E, Bindeman I (2009) Mass-independent isotopic signatures of volcanic sulfate from three supereruption ash deposits in Lake Tecopa, California. Earth Planet Sci Lett 282:102–114

Martin E, Bekki S, Ninin C, Bindeman I (2014) Volcanic sulfate aerosol formation in the troposphere. J Geophys Res Atmos 119:12660–12673

Matsuhisa Y, Goldsmith JR, Clayton RN (1978) Mechanisms of hydrothermal crystallization of quartz at 250 °C and 15 kbar.Geochim Cosmochim Acta 42:173–182

Mauersberger K (1981) Measurement of heavy ozone in the stratosphere. Geophys Res Lett 8:935–937

Mauersberger K, Erbacher B, Krankowsky D, Günther J, Nickel R (1999) Ozone isotope enrichment: Isotopomer specific rate coefficients. Science 283:370–372

Michalski G, Böhlke JK, Thiemens M (2004) Long term atmospheric deposition as the source of nitrate and other salts in the Atacama Desert, Chile: New evidence from mass-independent oxygen isotopic compositions. Geochim Cosmochim Acta 68:4023–4038

Michalski GM, Scott Z, Kabiling M, Thiemens MH (2003) First measurements and modeling of $\Delta^{17}O$ in atmospheric nitrate. Geophys Res Lett 30:1870

Morin S, Sander R, Savarino J (2011) Simulation of the diurnal variations of the oxygen isotope anomaly ($\Delta^{17}O$) of reactive atmospheric species. Atmos Chem Phys 11:3653–3671

Morton J, Barnes J, Schueler B, Mauersberger K (1990) Laboratory studies of heavy ozone. J Geophys Res 95:901–907

Röckmann T, Brenninkmeijer CA, Saueressig G, Bergamaschi P, Crowley JN, Fischer H, Crutzen PJ (1998) Mass-independent oxygen isotope fractionation in atmospheric CO as a result of the reaction CO + OH. Science 281:544–546

Savarino J, Thiemens MH (1999) Mass-independent oxygen isotope (^{16}O, ^{17}O, ^{18}O) fractionation found in H_x, O_x reactions. J Phys Chem A103:9221–9229

Savarino J, Bekki S, Cole-Dai J, Thiemens MH (2003) Evidence from sulfate mass independent oxygen isotopic compositions of dramatic changes in atmospheric oxidation following massive volcanic eruptions. J Geophys Res Atmos 108:4671

Schueler B, Morton J, Mauersberger K (1990) Measurement of isotopic abundances in collected stratospheric ozone samples. Geophys Res Lett 17:1295–1298

Sharma HD, Jervis RE, Wong KY (1970) Isotopic exchange reactions in nitrogen oxides. J Phys Chem 74:923–933

Sinha A, Lovejoy ER, Howard CJ (1987) Kinetic study of the reaction of HO_2 with ozone. J Chem Phys 87:2122–2128

Sofen ED, Alexander B, Steig EJ, Thiemens MH, Kunasek SA, Amos HM, Schauer AJ, Hastings MG, Bautista J, Jackson TL, Vogel LE, McConnell JR, Pasteris DR, Saltzman ES (2014) WAIS Divide ice core suggests sustained changes in the atmospheric formation pathways of sulfate and nitrate since the 19th century in the extratropical Southern Hemisphere. Atmos Chem Phys 14:5749–5769

Thiemens MH, Heidenreich HE (1983) The mass-independent fractionation of oxygen: A novel effect and its possible cosmochemical implications. Science 219:1073–1075

Thiemens MH, Jackson T, Zipf EC, Erdman PW, van Egmond C (1995) Carbon dioxide and oxygen isotope anomalies in the mesosphere and stratosphere. Science 270:969

Tsai S-M, Lyons JR, et al (2017) VULCAN: An open-source, validated chemical kinetics python code for exoplanetary atmospheres. Astrophys J Supp 228:2–28

Weston RE (1999) Anomalous or mass-independent isotope effects. Chem Rev 99:2115–2136

Winkler R, Landais A, Risi C, Baroni M, Ekaykin A, Jouzel J, Petite JR, Prie F, Minster B, Falourd S (2013) Interannual variation of water isotopologues at Vostok indicates a contribution from stratospheric water vapor. PNAS 110:17674–17679

Yeung LY, Affek HP, Hoag KJ, Guo W, Wiegel AA, Atlas EL, Schauffler SM, Okumura M, Boering KA, Eiler JM (2009) Large and unexpected enrichment in stratospheric $^{16}O^{13}C^{18}O$ and its meridional variation. PNAS 106:11496–11501

Young ED, Galy A, Nagahara H (2002) Kinetic and equilibrium mass-dependent isotope fractionation laws in nature and their geochemical and cosmochemical significance. Geochim Cosmochim Acta 66:1095–1104

Young ED, Yeung LY, Kohl IE (2014) On the $\Delta^{17}O$ budget of atmospheric O_2, Geochim Cosmochim Acta 135:102–125

Yung YL, DeMore WB, Pinto JP (1991) Isotopic exchange between carbon dioxide and ozone via $O(^1D)$ in the stratosphere. Geophys Res Lett 18:13–16

Yung YL, Lee AYT, Irion FW, DeMore WB, Wen J (1997) Carbon dioxide in the atmosphere: Isotopic exchange with ozone and its use as a tracer in the middle atmosphere. J Geophys Res 102:10857–10866

Zahn A, Franz P, Bechte C, Grooß J-U, Röckmann T (2006) Modelling the budget of middle atmospheric water vapour isotopes. Atmos Chem Phys 6:2073–2090